IEEE Access
Multidisciplinary | Rapid Review | Open Access Journal

Received April 15, 2020, accepted April 25, 2020, date of publication May 7, 2020, date of current version May 22, 2020.

Digital Object Identifier 10.1109/ACCESS.2020.2993078

Flexible Driving Mechanism Inspired Water Strider Robot Walking on Water Surface

JIHONG YAN, (Member, IEEE), KAI YANG, (Student Member, IEEE), GANGFENG LIU, (Member, IEEE), AND JIE ZHAO, (Member, IEEE)
State Key laboratory of Robotics and Systems, Harbin Institute of Technology, Harbin 150001, China

Corresponding authors: Jihong Yan (jhyan@hit.edu.cn) and Gangfeng Liu (liugangfeng@hit.edu.cn)

This work was supported in part by the National Natural Science Foundation of China under Grant 51775133, and in part by the National Defense Science and Technology Innovation Special Zone Project.

ABSTRACT The agile and efficient locomotion of water striders on water surface is attributed to the water repellency ability of their slender legs. The legs are usually treated as rigid beams, neglecting the effect of flexible deformation on its movement. Several studies proved that the stable floating ability of water striders is closely related to the flexible legs. This paper focuses on exploring the flexible driven mechanism between the insect and the surface of water and applied them to design a robot. The spatial deformation and force models of the driving legs are established and analyzed based on the Euler-Bernoulli's beam theory. The influence of flexural rigidity and depth of a driving leg on the rowing speed is studied. Results indicates that a flexible driving leg can effectively increase its critical rowing speed and ensure that it does not penetrate the water surface at a higher speed, thus achieving a bigger driving force. Then a water strider robot capable of walking on water surface is proposed, which possesses ellipse-like spatial trajectories by using a limit pin-linkage. The driving legs are fabricated by different stiffness materials. Finally, the skating experiments of the robots with different stiffness of the driving legs were carried out. The results verified that the maximum rowing frequency of the flexible driving legs and maximum moving speed of the robot are more than 30% higher than those with rigid legs, respectively. Moreover, a similarity analysis of hydrodynamic characteristic constants reveals that the flexible driving robot is more analogous to the biological water striders.

INDEX TERMS Flexible driving legs, miniature robot, surface tension, water strider.

I. INTRODUCTION

Aquatic creatures depending on surface tension driven method possess high agile and effective locomotion, which has an important inspiration for the exploration and development of surface tension driving technology. The waterlily beetle stands on the water surface exploiting surface tension of the air-water interface and moves by flapping its hind wings [1]. The mesovelia promotes itself by reducing the surface tension coefficient on one side [2], [3], which is called Marangoni effect. Water striders can float, walk and jump freely on water surface depending on the surface tension caused by the rowing of driving legs [4]–[7]. Miniature/micro water-walking robot inspired by water striders can be equipped to carry out various tasks such as water quality monitoring and aquatic search and rescue and has become a popular research focus.

The associate editor coordinating the review of this manuscript and approving it for publication was Hassen Ouakad.

Ever since Bush and Hu [8] designed the first robot mimicking the motion of water striders powered by elastic thread, a lot of robots imitating water striders are reported [5], [9]–[22]. Sitti *et al.* [10]–[12] designed a water strider robot driven by T-shaped actuation mechanism composed of three piezoelectric unimorph actuators, the legs are made of hydrophobic Teflon coated wires. They also studied the other two prototypes [13], [14]. Girad [15] designed a DC motor driven water strider robot which weighs about 20g. Wu *et al.* [16], [17] also fabricated two water strider robots powered by DC motor. Yan *et al.* [18] designed a water walking robot with a novel cam-link mechanism to mimic the ellipse-like spatial rowing trajectory of water strider's driving leg. Up to now, the reported surface tension-driven robots generally adopted rigid wires as support legs and driving legs, utilizing the hydrophobic coatings to improve the supporting force of the robots.

Studies have shown that when the contact angle (C.A) of material is greater than 90°, the maximum lifting force will

be almost the same regardless of the C.A [10]. Experimental observation shows that the legs of water striders have a small flexural rigidity. When supporting or rowing on water surface, the legs can bend into a small curvature shape to adapt to the deformation of water surface, which plays a key role in increasing the water-repellent ability [23]–[33]. Feng *et al.* [23], [24] investigated the deformation of the supporting legs on supporting force. They proved that the adaptive-deformation capacity of a real leg through its three joints plays a larger role than hydrophobicity in improving the supporting force. Vella [25] numerically analyzed the effect of bending deformation of a floating sender cylinder on supporting force and pointed out that the elastic leg exists an optimal length, below or above this length will result in the decrease in the support force. The result confirmed the research of Song and Sitti [10] on the load capacity of a compliant supporting leg. Through experiments, Kong *et al.* [26] proved that flexible supporting legs can effectively increase the supporting forces. Park and Kim [27] calculated the maximum depression of a flexible sheet before it pierces the water surface and demonstrated that a flexible sheet can support more load than a rigid one before sinking when the sheets are superhydrophobic. Koh *et al.* [33] found that in the jumping process, the end tip of the driving leg curved to maximize momentum transfer to water, and designed the first surface tension driven jumping robot with the end-curved superelastic shape memory alloy wires.

At present, the research on the leg flexibility of water striders is mainly focused on the support legs. The flexibility of driving legs has never been reported. However, based on the bionic prototype and the research results of flexible support legs, it is reasonable to assume that the flexibility of driving legs should greatly improve its rowing efficiency and locomotion stability.

In our previous work [34], flexible driving legs were designed based on bionic structure, then a robot was designed to verify the performance of flexible legs. Experimental results showed that flexible driving legs can achieve better performance. However, the deformation, force of flexible driving legs and the influencing factors have not been analyzed quantitatively. The actual deformation of a living driving leg when rowing is a complex space shape. And its vertical deformation has a great influence on the rowing speed. In this paper, the flexible driven mechanism is researched systematically. Spatial deformation model and force model of driving legs are developed. The dynamic behavior of the robot is analyzed through Matlab-ADAMS co-simulation method. The experimental and simulation results are compared and discussed deeply. The research results show that driving legs with a certain flexibility can effectively increase the walking velocity of a robot imitating water striders. And there exists an optimum stiffness for driving legs to maximize its movement performance. This paper can provide reference for optimization and functional application of water strider robots.

The rest of this paper is organized as follows. Section II introduces flexible driving mechanism and the modeling process of the flexible driving legs. In section III, a surface-tension-driven water strider robot is designed, a new limit pin-link mechanism capable of generating an ellipse-like spatial trajectory is proposed. In section IV, the rowing locomotion of the robot is analyzed through dynamic simulation. Then a robot prototype is fabricated, experiments are conducted by changing the stiffness and rowing frequency of the driving legs. Finally, hydrodynamic characteristic parameters are used to discuss the locomotion similarity between this surface tension-driven robot and a water strider.

II. FLEXIBLE DRIVING MECHANISM

A. ROWING PROCESS OF WATER STRIDERS ON WATER SURFACE

Fig. 1 illustrates the snapshots of the rowing process of a water strider [35]. The characteristic length and weight of an adult water strider is about 20 mm and 10 mg respectively. It has three pairs of legs, the front two legs are responsible for grabbing and auxiliary supporting. The hind legs are used to support the body. The middle pair is responsible for supporting when floating and rowing when walking or jumping on water surface. The cross-section diameter of the leg is about 0.1mm.

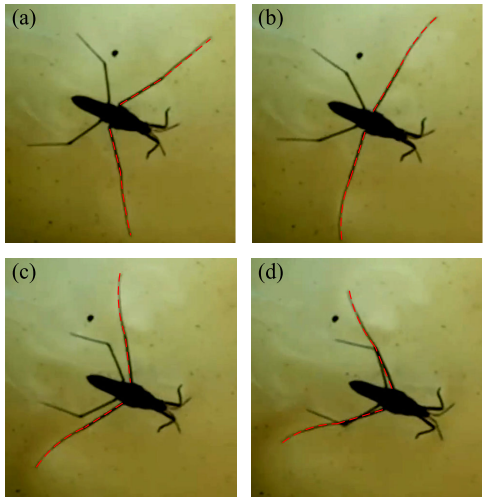

FIGURE 1. Deformation of the flexible driving legs when rowing [35].

The skating process of water striders can be divided into three stages according to the movement of middle legs: the rowing stage, swing back stage and inertial skating stage. Fig. 1 shows the completed rowing stage of a water strider. Its middle legs press on water surface (Fig. 1*a*) and swing backward rapidly (Fig. 1*b* and *c*). The surface tension and hydrodynamic pressure in the forward direction promote its body moving. The flexible legs are deformed in conformity with the water surface, as is shown by the red broken line in Fig. 1. At the end of the rowing stage (Fig. 1*d*), the middle legs begin to detach from the water surface to reduce the moving resistance, and are completely out of water surface when

entering the swing back stage. In the third stage, the middle legs fall back to the water surface, the body continues to skate by inertia. The middle legs possess an ellipse-like spatial trajectory, resulting in high water skating efficiency and low fluctuation on water surface.

B. DEFORMATION AND FORCE ANALYSIS

1) FLEXIBLE DRIVING LEG MODELING

The thin and long legs of water striders possess multi-section structure. Fig 2 (a) and (b) illustrate the schematic diagram of a water strider and structure of a driving leg respectively. The driving leg can be divided into coxa, femur, tibia and tarsus and anterior tarsus. When rowing, the driving legs depress into the water surface with a certain depth, part of the femur and the whole tibia are in contact with the water surface. The forces exerted on the tarsus segment and anterior tarsus segment can be ignored since they are small in size. The simplified driving leg model is built as is shown in Fig. 2 (c). Here we assume that the depth of the driving leg when rowing is h_1 and the angle between femur and tibia is γ.

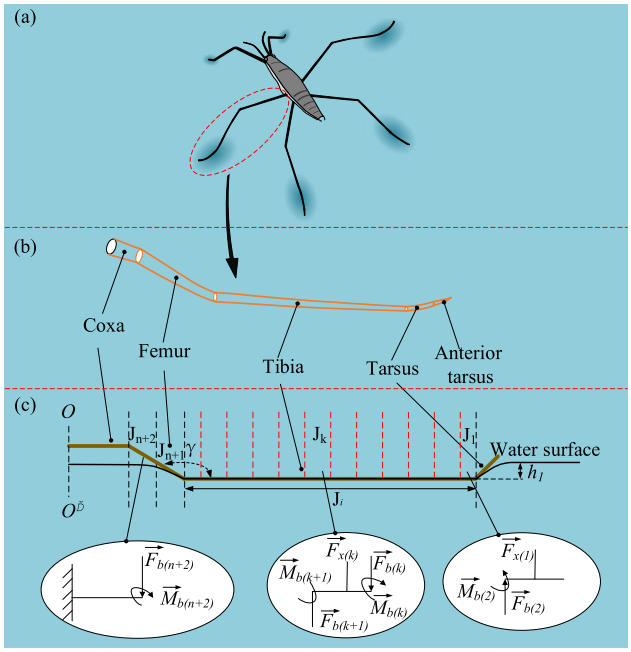

FIGURE 2. Deformation model of flexible driving legs.

For a rigid driving leg, its shape remains unchanged during the rowing process. Due to the flexural rigidity, a flexible driving leg will deform in horizontal direction and vertical direction. In order to explore its deformation characteristics, the above-mentioned driving leg structure was analyzed based on Euler-Bernoulli beam theory. Since the forces exerted on per unit length of the leg vary with the rowing velocity and depth, the leg is divided into discrete segments according to the forces.

The coxa is connected to the body of the robot and almost no deformation occurs. The femur is divided into two parts, the part above water surface and the part under the water surface, according to its depth. The tibia is the main component of the driving leg rowing on the water surface and is divided into n beam segments with equal length. The translational velocity of a beam unit is assumed to be the velocity of the center of the segment, rotation velocity of the segment is not considered.

As is shown in Fig. 2 (c), the forces exerted on each beam segment J_k includes the force $F_{x(k)}$ caused by itself (sum of the surface tension, hydrostatic force, hydrodynamic force and viscosity resistance), the resultant force $F_{b(k)}$ and resultant moment $M_{b(k)}$ of all the beam elements on the lateral side (exerted on the end tip of segment k), the balance force $F_{b(k+1)}$ and balance moment $M_{b(k+1)}$ (exerted on the front tip of the element). Specially, the forces exerted on the element J_{n+2} only contains the resultant force $F_{b(k+2)}$ and resultant moment $M_{b(k+2)}$ of all the lateral units since it's above the water surface.

2) FORCE MODELING

When a cylindrical leg rowing parallel on water, the interaction between the leg and water surface comprises four parts: surface tension (F_σ), hydrostatic pressure (F_b), hydrodynamic pressure (F_d) and viscosity resistance (F_v). The forces can be divided into three mutually perpendicular directions, as is illustrated in Fig. 3 (a).

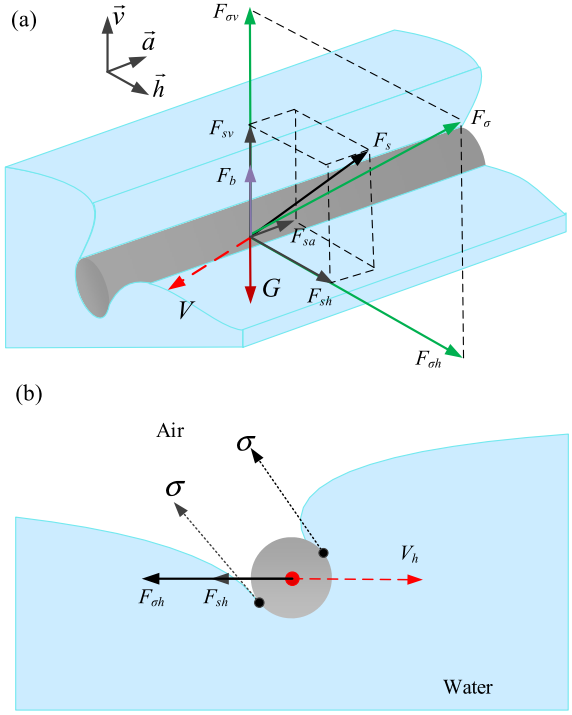

FIGURE 3. (a) Forces exerted on the element of flexible driving leg and (b) Surface tension force model in the horizontal direction.

Force analysis is the base of robot design. Scholars have carried out a lot of theoretical and experimental research on the forces acting on the legs of water striders [36]–[39]. Combine our previous work [18], the force in the axial

direction F_a, composed of dynamic pressure and viscosity resistance. The force in the vertical direction F_v can be simplified to the sum of the lifting force corresponding to a quasi-static state and vertical velocity-induced resistance. The horizontal force perpendicular to the axis F_h was also approximately divided into two forces: the component of surface tension force in the horizontal plane($F_{\sigma h}$) and the sum of hydrodynamic force and viscosity resistance (F_{sh}). The resultant forces in the three in three directions can be expressed as

$$\begin{cases} F_a = \frac{1}{2}\int_S c_a \rho V_a^2 \mathrm{d}S \\ F_v = \int_l (25.9 - 45.3h_o)dl + \frac{1}{2}\int_S c_v \rho V_v^2 \mathrm{d}S \\ F_h = \int_l \lambda\sigma\, dl + \frac{1}{2}\int_S c_h \rho V_h^2 \mathrm{d}S \end{cases} \tag{1}$$

where c_v, c_a and c_h are the resistance coefficients in three directions. V_v, V_a and V_h are the components of rowing velocity in three directions. ρ is the density of water. h_o, l and S are the depth, length and leg-water contact area, respectively. λ is a dimensionless coefficient. σ is the coefficient of surface tension. To facilitate lifting force calculation, the lifting force exerted on a leg with a diameter of 0.8 mm, including the surface tension and hydrostatic force, are fitted by a straight line as a function of depth h, as denoted by the first item of F_v. The contact angle of the leg are 155°.

Fig. 3 (b) shows the forces exerted on a driving leg in the horizontal direction, before penetrating into the water surface, the surface tension force per unit length in the horizontal direction ranges from 0 to 2σ, so the dimensionless coefficient λ ranges from 0 to 2. And it is related to the cross-sectional size, surface wettability, rowing velocity and depth of the leg. Before the water surface is pierced, the higher the rowing velocity and the deeper the stroke depth, and the larger the value of λ is. Here we suppose that λ has a linear relationship with the rowing velocity before the leg breaks the water surface, then λ can be expressed as:

$$\lambda = \begin{cases} 2 \times V_h / V_{max} & V_h \le V_{max} \\ 0 & V_h > V_{max} \end{cases} \tag{2}$$

where V_{max} is the critical horizontal rowing velocity before a leg pierces water surface, depending on its depth h.

To make (2) solvable, referred to our previous work [18], a simple 2D model was proposed to correlate V_{max} with the rowing velocity and depth, as is illustrated in Fig. 4. Ignoring the effects of fluid flow in the fluid region A, in a quasi-static critical state, a thin and long cylinder rows on water surface, the forces exerted on the water area A approximately fulfills the following equilibrium equation

$$\frac{1}{2}\rho_l g h^2 - \frac{1}{2}\rho_l V_{\max}^2 h = \sigma_1 + \sigma_2 = 2\sigma \tag{3}$$

where g is the gravity acceleration, h denotes the distance between three phase contact line and free water surface, and it can be expressed as $h_0 + r$ in terms of which h_0 is the depth of the center of the cylinder leg, r is the radius of cylinder. ρ_l is the density of water. Refer to (3), the first and second term on the left side are hydrostatic pressure and hydrodynamic pressure respectively.

Equation (3) illustrates that a cylinder can row at the air-water interface if the water pressure is less than 2σ. Otherwise, the surface tension caused by the cylinder and free water surface can no longer withstand the water pressure, the water surface will be pierced and the cylinder will be submerged in the water completely. Then the critical velocity could be calculated

$$V_{max} = \sqrt{\frac{\rho_l g h^2 - 4\sigma}{\rho_l h}} \tag{4}$$

Fig. 4 illustrates the change of critical rowing velocity of a driving leg with its depth. It can be seen that the critical velocity decreases with the increase of depth.

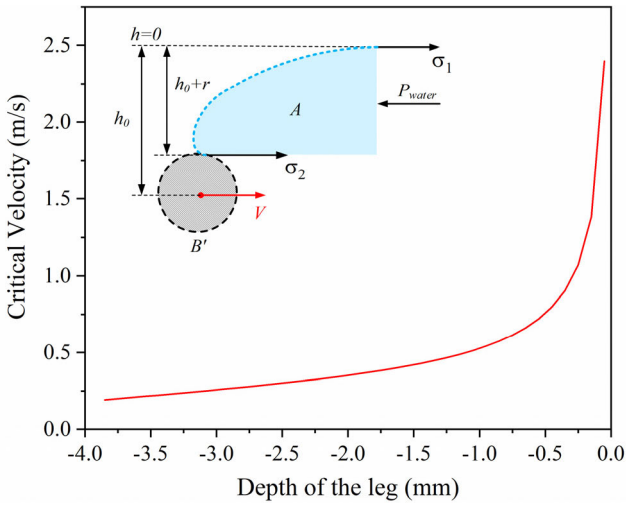

FIGURE 4. Numerically calculated critical rowing velocity for legs with its depth.

3) DEFORMATION OF DRIVING LEGS

When a flexible driving leg rows on water surface, its deformation is a complex spatial deformation. To simplify the problem, the deformation is decomposed into the vertical deformation caused by the hydrostatic pressure and the surface tension, and the horizontal deformation caused by hydrodynamic water pressure and surface tension, as is shown in Fig. 5. In the figure, the broken line $\overline{OAC}$ denotes a rigid driving leg rowing in depth h and no deformation occurred. OO' is the rotation axis of the driving leg. The curve $\overset{\frown}{AB}$ denotes the spatial deformation of a flexible driving leg with a certain angular velocity (ω). $\overset{\frown}{A'B}$ and $\overset{\frown}{AB'}$ are the projection of the deformation in the vertical plane yz and the horizontal plane xy respectively. Δl_v and Δl_h are the maximum deflection of the vertical and horizontal deformation of the flexible leg, separately.

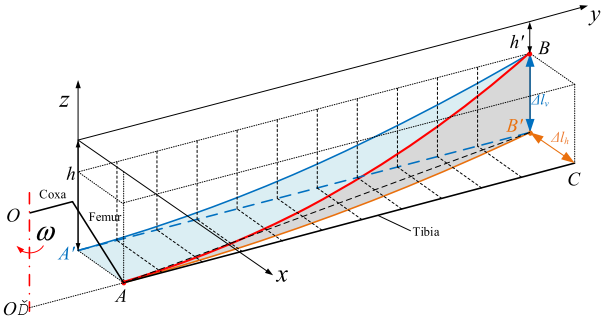

FIGURE 5. Schematic diagram of a driving leg when rowing on water surface.

a: DEFORMATION IN THE VERTICAL DIRECTION

The deformation of a driving leg in the vertical direction is mainly caused by surface tension and hydrostatic force. As shown by the curve $\overset{\frown}{A'B}$ in Fig. 5, the farther away from the rotation axis of the leg, the bigger the deflection.

The forces exerted on each unit of the leg vary with its depth. After the first computing of vertical deformation, the depth of each beam unit of the leg will change, resulting in the change of the forces. It's impossible to achieve the stable deformation in one time. So here the iterative calculation method is hired to calculate the vertical deformation. The deflection and deflection angle of each beam unit can be solved based on Euler-Bernoulli beam theory once the leg parameters (including the structure and material parameters) and initial depth (h_0) are given. When the new depth of each beam unit is achieved, the depth difference of each segment in two adjacent steps is calculated, if all of the depth differences are less than 0.01mm, the stable deformation is achieved and the calculation is ended. If not, the calculation continues.

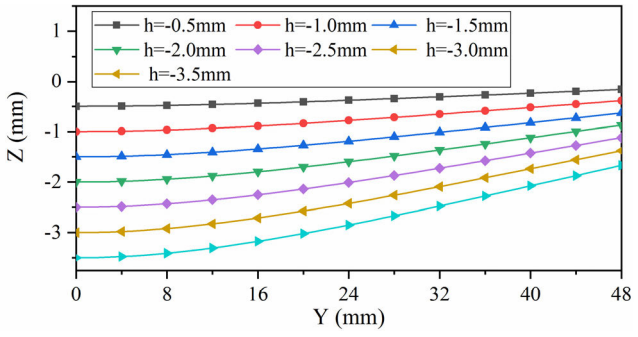

FIGURE 6. Numerically calculated vertical deformation of driving leg in different depth.

Fig. 6 illustrates the vertical deformation of a thin and long flexible cylinder leg (made of Acrylonitrile Butadiene Styrene (ABS) material) in different depth. Its diameter and length are 0.8 mm and 48 mm respectively, and its elastic modulus is 2.3 GPa. Since the maximum depth of a hydrophobic coated wire is usually smaller than 4 mm, here the depth ranges from −0.5 mm to −3.5 mm with an interval of −0.5 mm. It can be seen that the deformation increases with the depth of the leg, the maximum deflection is 0.645 mm and 1.93 mm when the depth of the leg is −1 mm and −3.5 mm, respectively.

For a rigid leg ($\overline{OAC}$), no deformation occurs, the end tip (C) and the base tip (A) have the same depth h. When the leg rows on water surface with an angular velocity ω, the velocity of point A and C can be expressed as:

$$\begin{aligned} V_A &= \omega l_{O'A} \\ V_C &= \omega l_{O'C} \le V_{h\_\max} \end{aligned} \tag{5}$$

where $l_{O'A}$ denotes the distance of the base tip to the rotation center of the leg (O'), $l_{O'C}$ is the distance between the end tip and rotation center. It can be seen that the end tip has a larger rowing velocity and is easier to exceed the maximum rowing velocity (V_{h_max}) in depth h and break the water surface.

For a flexible driving leg with the same parameters and depth, due to the passive deformation, the rowing velocity of the end tip (B) can be described as

$$V_{\mathrm{B}} = \omega l_{OB} \le V_{h'\_\max} \tag{6}$$

where l_{OB} is the straight-line distance between the end tip of deformed leg (B) and point O. Due to the deformation, l_{OB} is smaller than $l_{O'C}$.

$$l_{OB} < l_{O'C} \tag{7}$$

The actual depth of the end tip h' is smaller than a rigid one (h). According to Fig. 5, Then we got

$$V_{h\_\max} < V_{h'\_\max} \tag{8}$$

According to (5)-(8), we can see that a flexible driving leg can row on water with a bigger rowing velocity without penetrating into the water surface.

b: DEFORMATION IN THE HORIZONTAL DIRECTION

For a flexible driving leg, there exists a coupling relationship between its vertical deformation and horizontal deformation. It's difficult to verify the change of the forces, especially the surface tension, in the two directions. To make the horizontal deformation solvable, in this study, we suppose that the vertical deformation of the leg remains unchanged when the driving leg rows on water surface. When computing the surface tension in the horizontal plane by (2) and (4), the critical rowing velocity of each segment is computed using its local depth after the vertical deformation.

Fig. 7 (a) shows the schematic diagram of flexible driving legs rowing on water surface. The swing range of the driving leg in the horizontal direction is about 73°, here we define the angle perpendicular to the forward direction of the body as 0°. The brown broken line *1* and *2* are the two extreme positions of the driving leg, the corresponding angles are 30° and −43° respectively. The blue dotted line denotes the horizontal deformation of a flexible driving leg, the green broken line is a rigid leg at the same swing angle.

For the flexible leg, the horizontal rowing velocity of the i-th segment ($i = 1$, the end tip shown in the figure) V_{Fi} can

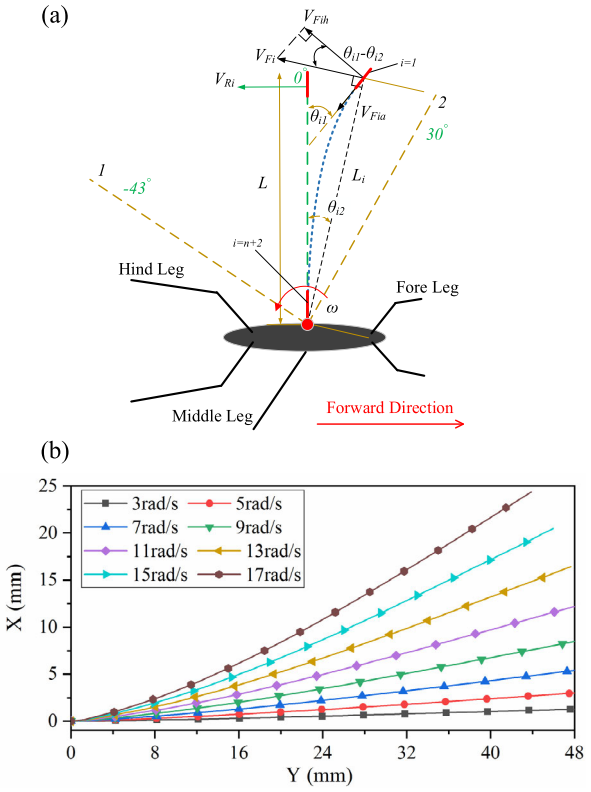

FIGURE 7. (a) Horizontal deformation of the actuating leg when rowing, the blue dotted line denotes the horizontal deformation of a flexible driving leg, the green broken line is a rigid leg at the same swing angle, and (b) numerically calculated horizontal deformation of a driving leg in different rowing angular velocity, the depth of the leg is 1mm and the corresponding vertical deformation is illustrated by the red line in Fig. 6.

be divided into a normal component V_{Fih} (vertical to the axis direction of the i-th segment) and a tangential component V_{Fia} (the axis direction of the i-th segment).

For the rigid leg, the velocity of the i-th segment V_{Ri} is always vertical to the axis of the leg. By neglecting the decrease of the leg length due to the deformation, then we got

$$V_{Fi} = V_{Ri} = \omega L_i \tag{9}$$

where ω is the rowing angular velocity of the driving leg, L_i is the length of connection line of the midpoint of the i-th segment and the rotation center. For the deformed leg as shown in Fig. 7 (a), θ_{i1} is the angle between the axial direction of the i-th segment and the undeformed leg. θ_{i2} is the angle between the connection line and the undeformed leg. Then the normal component V_{Fih} can be solved:

$$V_{Fih} = V_{Fi} \times \cos(\theta_{i1} - \theta_{i2}) \tag{10}$$

The deformation of the air-water interface is mainly caused by the velocity component vertical to the axis direction of a segment, the axial velocity component plays little effect. Once the velocity vertical to the axis direction exceeds the critical rowing velocity, the water surface will be pierced. Since $\cos(\theta_{i1} - \theta_{i2}) < 1$, V_{Fih} is always smaller than V_{Ri}. That means a rigid leg is easier to pierce the water surface than a flexible one, flexible legs can row on water surface faster. Based on the Euler-Bernoulli beam theory, the forces and deformation of each segment can be expressed by (11) and (12), respectively.

$$\begin{cases} F_i = \lambda l_i \sigma + 0.5 S \rho_l C_s V_i^2 \cdot \cos(\theta_{i1} - \theta_{i2}) \\ F_{bi} = \sum_{i=1}^{i-1} F_i \\ M_{bi} = \sum_{i=1}^{i-1} M_{bi} + F_i \cdot \dfrac{l_i}{2} + F_{bi} \cdot l_i \end{cases} \tag{11}$$

$$\begin{cases} w_i = \left(5F_i l_i^3/48 + M_{bi} l_i^2/2 + F_{bi} l_i^3/3\right)/E/\mathrm{I} \\ \theta\theta_i = \left(F_i l_i^2/8 + M_{bi} l_i/ + F_{bi} l_i^2/2\right)/E/I \end{cases} \tag{12}$$

where F_i is the total force exerted on the center of segment i in the horizontal direction. C_s denotes the resistance coefficient. M_{bi} is the balance moment exerted on the end tip of segment i, l_i, w_i and $\theta\theta_i$ indicate the length, deflection and deflection angle of the segment, separately. E and I are the elastic modulus of the leg material and the moment of inertia of the cross section, respectively.

When the flexible driving leg rows on water surface at a certain angular velocity, the horizontal deformation of the leg will result in the change of the rowing velocity of each segment, which affects its horizontal forces. Similar to the calculation method of vertical deformation, the horizontal deformation of the flexible leg is also solved by the iterative calculation method, until the position difference of each segment in two adjacent steps is less than 0.01mm. Fig. 7 (b) illustrates the horizontal deformation of ABS material driving legs, the depth of the leg is 1 mm, and its vertical deformation is illustrated by the red line in Fig. 6. The structure parameters of the ABS material leg is the same as the previous section. It can be seen that the horizontal deformation increases with the rowing velocity.

c: CRITICAL ROWING VELOCITY AND DRIVING FORCE OF A FLEXIBLE LEG

The previous analysis has given the deformation and forces calculation methods of a flexible leg. Then the maximum rowing velocity and driving force of a driving leg with different material, diameter, depth and length *et al.* can be numerically solved. The method is: for a leg with a certain depth, continuously increase the rowing velocity of the leg with an interval of 0.01 rad/s, and compute its forces and spatial deformation, then check whether the maximum rowing velocity of each segment exceeds the critical value of the segment in the corresponding depth. If so, the computation will ended, or the computation continues.

Fig. 8 shows the maximum rowing angular velocities and maximum driving force of ABS material, copper and ideal rigid driving legs varying with the depth. The corresponding elastic modulus of the ABS material, copper are 2.3 GPa and 90 GPa respectively. The structure parameters of the driving leg are also illustrated.

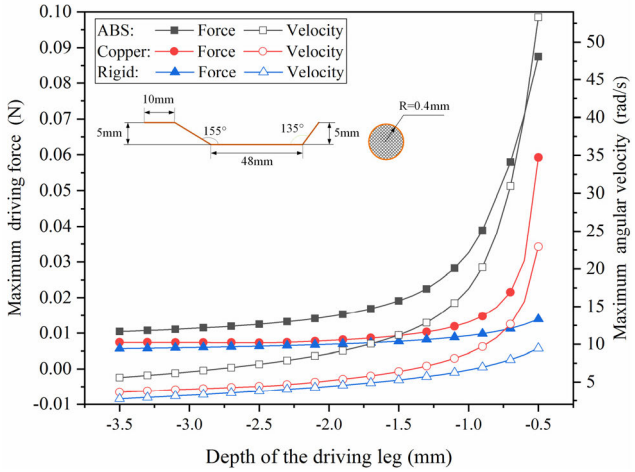

FIGURE 8. Maximum rowing speed and force of driving legs in different depth.

It can be seen that the maximum rowing angular velocity decreases with the increase of the depth. In the same depth, the ABS material leg can achieve the biggest rowing angular velocity, thus a bigger driving force than a rigid leg. The numerical solution, along with the theoretical analysis results, suggests that flexible driving legs can row on water surface with a larger velocity due to its horizontal and vertical deformation. It's worth nothing that, if the stiffness of a driving leg decreases continuously, the deformation will be too large to provide sufficient driving force. So there exists an optimum stiffness for the driving legs. But limited by the materials and fabrication method, the stiffness of an elongated and flexible leg can hardly to be changed randomly, here we only analyzed the flexible legs with an elastic modulus of 2.3GPa.

III. FORCE MODELLING AND ROBOT DESIGN

To design a surface-tension-driven robot, the following principles should be met: (1) the robot should be light enough so that the surface tension dominates the supporting force. (2) the driving legs row on the air-water interface in the rowing stage and then detach form water in the swing back stage to decrease the resistance force. Fig. 9 (a) shows the sketch of the miniature surface tension-driven robot. It consists of a body, ten supporting legs and two actuating legs. Each actuating leg is fixed on the rocker of a four-link mechanism driven by a DC motor through a group of reduction gears. The two DC motors are connected with a control circuit via four external wires.

A. DRIVING MECHANISM DESIGN

In order to achieve the ellipse-like spatial trajectory, the drive mechanism is designed by a combination of a four-link mechanism and limit pin mechanism. The four-link mechanism enables the actuating legs to switch back and forth in the horizontal plane, meanwhile the limit pin is used to turn over the driving legs in the two extreme positions and create the up-down motion, as shown in Fig. 9 (b).

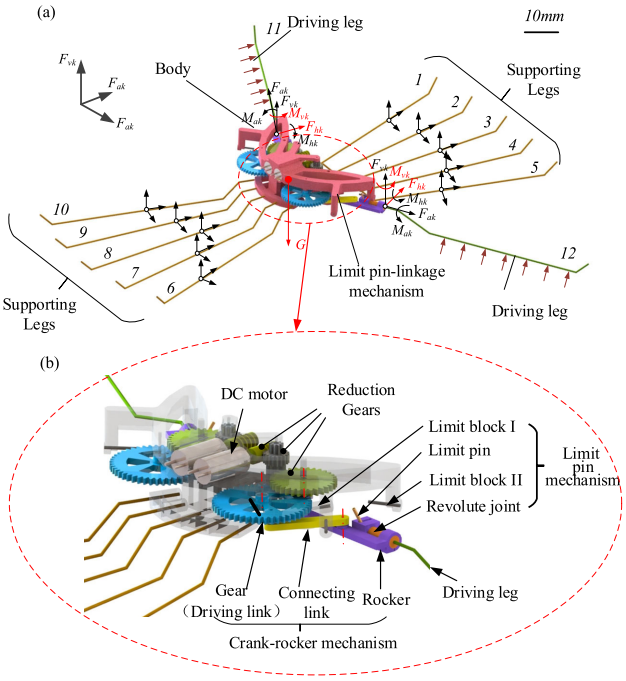

FIGURE 9. (a) CAD model of the miniature water-walking robot, No.1∼10 are supporting legs, No.11, 12 are driving legs, and (b) the driving mechanism.

TABLE 1. Parameters of the four-link mechanism.

LINK	Length (mm)
Driving link	4
Fixed link	8.4
Rocker	9
Connecting link	11

The two simultaneous motions synergize to generate an ellipse-like spatial trajectory. For water striders, the swing range of actuating legs is 73°, so the dimension parameter of the four-link mechanism is designed, as shown in Table 1, the corresponding swing range of the mechanism is 73°. When compared with the former cam-link driven prototype [18], only driving legs rotates at the two extreme positions, the height and position of the driving mechanism maintain unchanged, so the new prototype consumes less power when the driving legs detach from water surface.

Fig. 10 illustrates the ellipse-like spatial trajectory of the center of driving leg. It consists of the water entry and exist, swing back and rowing on water surface, according to the depth of the leg. When the leg rotate to the two extreme positions, the limit pin rotates around the axis by the interaction force F caused by the limit blocks, resulting in the water entry and exit of the driving leg. It is worth noting that when the driving leg rows on water surface, the driving force caused by water surface is constrained by the left side of the limit pin and no rotation occurred during the rowing process.

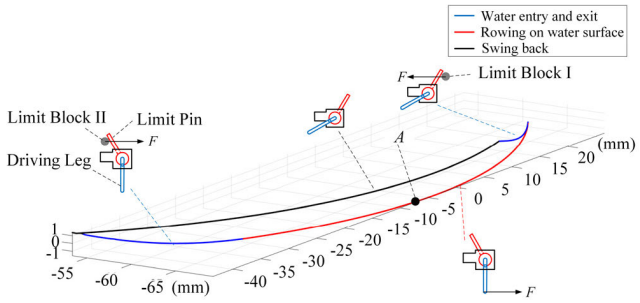

FIGURE 10. The ellipse-like spatial trajectory of the actuating leg.

B. SUPPORTING SYSTEM DESIGN

In order to ensure that the designed robot has enough load capacity, the robot adopts a plurality of elongated support legs arranged in a radial shape to increases the total length of the support legs.

The appropriate amount, arrangement and spacing of supporting legs are important for the load capacity and stability of the robot. If the gap between two adjacent driving legs is too large, the supporting force decreases while the resistance increases. If the spacing is too small, the width of the robot decreases, which may reduce its stability. In our previous work [40], the supporting force of a multiple slender cylinders floating on water surface has been analyzed. Refer to the method, the supporting legs system is carefully designed. The number of robot support legs is designed to be 10. The spacing between two adjacent legs is 10 mm. The maximum depth of the support leg is 3.6 mm, in this case, the supporting force obtained is about 80 mN, and the weight of the robot designed is about 50 mN. The load margin is more than 60%, so that even if the prototype is tilted due to water fluctuation in the moving process, the robot can still obtain sufficient lifting force to stay on the water surface.

IV. DYNAMIC ANALYSIS

A. DYNAMIC MODEL

Ignoring the air resistance, the forces exerted on supporting legs can be equivalent to three forces (F_{vk}, F_{ak} and F_{hk}) in mutually perpendicular directions acting on the leg center. The forces are expressed as

$$\begin{cases} F_{ak} = \dfrac{1}{2}\displaystyle\int_{S_k} c_{a_k}\rho V_{a_k}^2 \,\mathrm{d}S_k \\ F_{vk} = \displaystyle\int_{l_k} (25.9 - 45.3h_{o_k})dl_k + \frac{1}{2}\int_{S_k} c_{v_k}\rho V_{v_k}^2 \,\mathrm{d}S_k \\ F_{hk} = \displaystyle\int_{l_k} \lambda_k \sigma dl_k + \frac{1}{2}\int_{S_k} c_{h_k}\rho V_{h_k}^2 \,\mathrm{d}S_k \end{cases} \quad (13)$$

where k is the number of the support legs, which varies from 1 to 10, as is shown in Fig. 9(a).

The forces exerted on a flexible driving leg is a non-uniform load, and it can be equivalent to three forces (F_{ak}, F_{vk} and F_{hk}, $k = 11, 12$) and three torques (M_{ak}, M_{vk} and M_{hk}, $k = 11, 12$) acting on the end tip of the rocker, as is shown in Fig. 9 (a). The forces and torques can be found as

$$\begin{cases} F_{ak} = \displaystyle\sum_{i=1}^{N+1} (\frac{1}{2} c_{a_k}\rho S_{ik} V_{ia_k}^2) \\ F_{vk} = \displaystyle\sum_{i=1}^{N+1} (25.9 - 45.3h_{i_k}) l_{ik} + \sum_{i=1}^{N+1} (\frac{1}{2} c_{v_k}\rho S_{ik} V_{iv_k}^2) \\ F_{hk} = \displaystyle\sum_{i=1}^{N+1} [\lambda_{ik}\sigma l_{ik} + \frac{1}{2} c_{h_k}\rho S_{ik} V_{ih_k}^2] \\ M_{ak} = 0 \\ M_{vk} = \displaystyle\sum_{i=1}^{N+1} [(25.9 - 45.3h_{i_k}) l_{ik} + \frac{1}{2} c_{v_k}\rho S_{ik} V_{iv_k}^2] d_{ik} \\ M_{hk} = \displaystyle\sum_{i=1}^{N+1} [\lambda_{ik}\sigma l_{ik} + \frac{1}{2} c_{h_k}\rho S_{ik} V_{ih_k}^2] d_{ik} \end{cases} \quad (14)$$

where i denotes the number of the segment of a flexible leg. d_{ik} is the distance between the center of the i-th segment and the end tip of the rocker. Then the equation for the robot's motion on water surface can be expressed as:

$$\begin{cases} ma = \displaystyle\sum_{k=1}^{12} (F_{ak} + F_{vk} + F_{hk}) - G \\ I\alpha = \displaystyle\sum_{k=1}^{12} \left((F_{ak} + F_{vk} + F_{hk}) \times \vec{\chi}_k \right) \\ \qquad + \displaystyle\sum_{k=11}^{12} (M_{ak} + M_{vk} + M_{hk}) \end{cases} \quad (15)$$

where m is the mass of the robot, a and α are the acceleration and angle acceleration at the center of gravity, respectively. I is the robot's moment of inertia, and $\vec{\chi}_k$ is the displacement vector between the point of force and the gravity center of the robot.

To clarify the influence of the flexible driving legs on the performance of the robot, the dynamic properties of the robot were analyzed by ADAMS. For a flexible driving leg, due to the nonlinearity of the deformation, the driving forces can only be solved through numerical method, which is difficult to be solved in Adams. So the Matlab/Adams co-simulation method is employed. Matlab software is used to solve the deformation and forces exerted on each flexible driving leg according to its rowing velocity, depth and position. Then the numerically solved forces and torques are imported to Adams to simulate the kinetics behavior.

B. SIMULATION OF THE ROBOT AT THE CRITICAL ROWING FREQUENCY

When the robot statically stands on the water surface, the depth of driving legs is about 1mm. According to Fig. 8, the critical rowing angular velocities of ABS material and copper driving legs are 17.25 rad/s and 9.03 rad/s. Taking into account the characteristics of the crank linkage mechanism, the maximum rowing frequency of the robot are 2.57 Hz and 1.35 Hz respectively. Fig. 11 shows the simulation results of

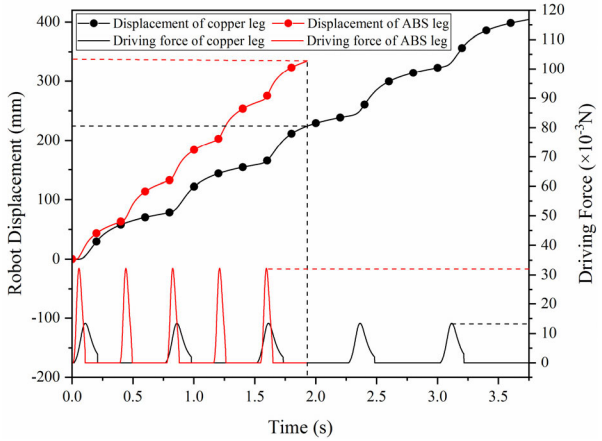

FIGURE 11. Simulation results of the robot with ABS material and copper driving legs (rows 5 cycles at the maximum rowing frequency).

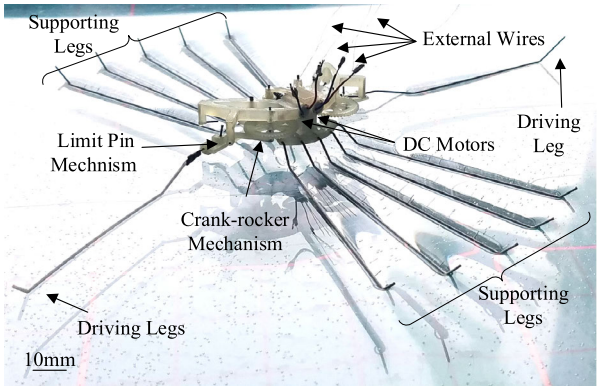

FIGURE 12. Photo of the final fabricated miniature water-walking robot prototype.

the robot rowing 5 cycles at the maximum rowing frequency. The average forward speed of the robot with ABS material and copper leg is 172.5 mm/s and 107.6 mm/s. The figure also illustrates the forces exerted on the driving legs. It can be seen that ABS material leg can achieve a bigger driving forces before penetrating the water surface.

V. EXPERIMENTS AND DISCUSSION

The new surface tension-driven robot was fabricated as shown in Fig. 12. The robot weighs 4.9 g and its total length, width and height are 160mm, 195mm and 16mm respectively. The main frame and parts of the reduction gears were fabricated by 3D printing techniques to reduce the robot's weight. The rotating shafts and the limiting rods are made of carbon fiber rods. The supporting legs are made of superhydrophobic copper tubes with a diameter of 0.5 mm. By controlling the motions of the two actuating legs, the robot can move on a water surface in different modes. PWM method, an approach for input voltage regulation by changing duty cycle, was applied to achieve the rowing frequency control of the actuating legs. The flexible and rigid driving legs are made of ABS material and copper material with a diameter of 0.8mm, the detailed structure parameters of the leg is illustrated in Fig. 12. The flexible legs are also fabricated by 3D printing techniques. The elastic modulus of the legs is 2.3 GPa.

The skating experiments include linear motion experiment and turning motion experiment. For the linear motion experiment, the two driving legs row synchronously and drive the robot moving linearly. For the turning motion experiment, the left driving leg rows with different frequencies while the right driving leg is fixed at the midpoint *A* of the rowing trajectory in Fig. 10. The average forward and turning velocities are calculated. The rowing experiments were carried out with ABS and copper driving legs, and the structure parameters of the legs are the same as the analysis in Fig. 8.

A. FORWARD MOTION EXPERIMENTS

Fig. 13 shows the linear motion of the ABS material driving leg at a frequency of 1.5 Hz. As can be seen from the figure, the flexible driving leg is deformed in conformity with the water surface during the rowing stage, and the driving legs detach from the water surface during the swing back stage.

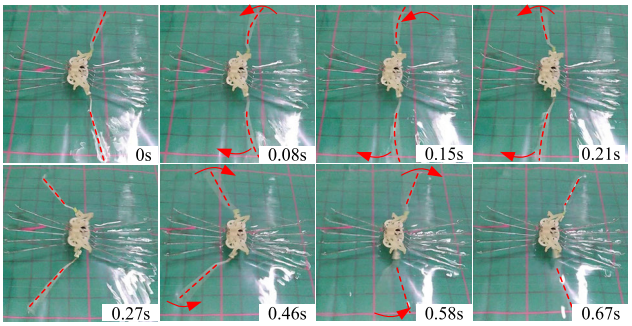

FIGURE 13. Snapshots of the forward motion experiment.

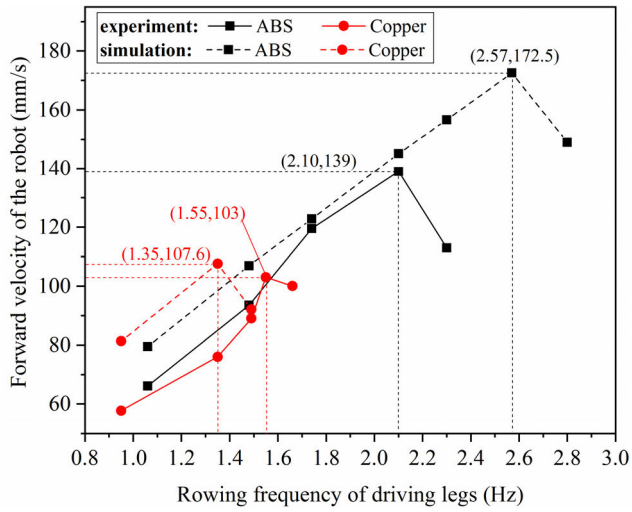

FIGURE 14. Experimental and simulation results of forward motion.

The forward motion experiment results are shown in Fig. 14. The maximum rowing frequency of copper legs and ABS material legs were measured to be 1.55 Hz and

2.10 Hz, the corresponding forward speeds were 103 mm/s and 139 mm/s respectively. The maximum rowing frequency of the ABS material driving legs and maximum moving speed of the robot are about 35.5% and 34.9% higher than those of the robot with copper legs. The rowing frequency exerts a positive effect on the velocity of the robot before the driving legs penetrate water surface. Once the rowing frequency exceeds the maximum rowing frequency, the water surface will be pierced by the driving legs, the forward speed of the robot decreases. This is because that the surface tension drops rapidly in the rowing process while the drag force when the driving legs detaches from water surface increases. Since the maximum rowing frequency of the driving legs and the skating velocity of the robot are the two key indexes we concerned, the skating experiments with higher rowing velocities are not conducted.

Fig. 14 also shows the simulation results of the robot at different rowing frequencies. Before penetrating into the water surface, the maximum forward speed of the robot with copper legs and ABS material legs are 107.6 mm/s and 172.5 mm/s, respectively. The simulation results show the same trend when compared with the experimental results. As described above, once the rowing frequency exceed the numerically calculated maximum value, the water surface will be pierced and the leg will be submerged into the water. So in the simulation, the surface tension is excluded from the propulsion force.

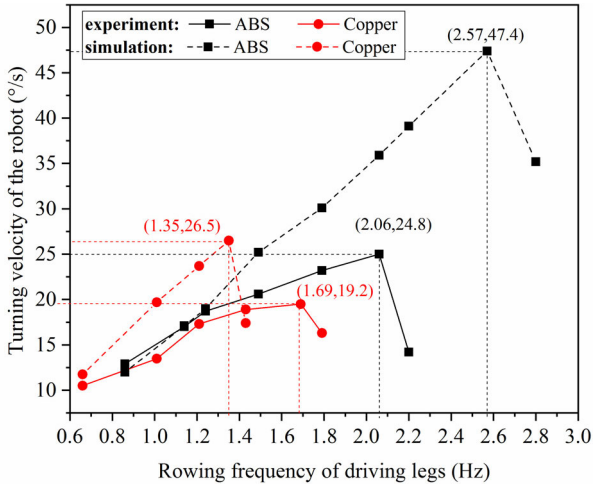

FIGURE 15. Experimental and simulation results of turning motion.

B. TURNING MOTION EXPERIMENTS

Fig. 15 shows the turning motion experimental and simulation results of ABS material driving legs, from which it can be seen that the rowing frequency exerts a positive effect on the velocity of the robot. Similar to the forward motion, once the frequency exceeds the maximum rowing frequency, the turning speed of the robot decreases. The maximum rowing frequency of Copper and ABS material was measured to be 1.69 Hz and 2.06 Hz, the corresponding turning speed was 19.2 °/s and 24.8 °/s respectively.

For ABS material legs, the numerical maximum rowing frequency is 2.57 Hz, which is bigger than the experimental results. While the simulated maximum rowing frequency of copper legs is 1.35 Hz, which is a little smaller than the experimental results. The possible reasons are as follows: (1) the deformation model and critical rowing velocity model of flexible legs are inaccurate. The spatial deformation of a flexible driving leg rowing on water surface is complicated, to make the problem solvable, the deformation is divided into a horizontal and vertical deformation. The maximum rowing velocity is based on a quasi-static force model. (2) When calculating the numerical maximum rowing frequency, the absolute velocity is adopted, for the actual driving legs on a robot skating on water surface, rowing velocity of driving legs may be partially offset by the forward or turning speed of the robot, so that the robot can row with a higher frequency.

Whether the forward motion or the turning motion, the simulation results are a little bigger than the experimental results. The error may be caused by two main factors: (1) The force models of the driving legs and supporting legs are not accurate enough. (2) The external wires cause some resistance. The results also show that for the same rowing frequency, the robot equipped with copper driving legs runs faster than the one with ABS material legs, which means that driving forces of rigid legs are bigger than flexible legs. So we can got the following conclusion: the advantage of flexible driving legs is to increase the average rowing velocity of the legs, thus generate a larger driving force. Its driving force at the same rowing speed is smaller than a more rigid leg.

C. COMPARISON TO WATER STRIDERS

The hydrodynamic dimensionless parameters are adopted to describe similarity of locomotion between the robot and a water strider (∼0.01 g). Table 2 lists geometric, dynamic and dimensionless parameters. Bond Number ($Bo = \rho g L^2/\sigma$) denote a ratio of the hydrostatic pressure to surface tension [21]. The smaller the parameter, the more dominant role the surface tension plays.

TABLE 2. Geometric, dynamic and dimensionless parameters.

	L (mm)	U (m/s)	Bo
Robot with rigid driving legs	0.8	0.46	0.087
Robot with flexible driving legs	0.8	0.62	0.087
Water Strider	0.1	0.7	0.001

L and U denote the characteristic length and velocity, respectively. For this robot, L equals the cross-section diameter of the actuating leg, and U is the midpoint velocity of the actuating leg's rowing segment. Compared the prototype with rigid and flexible driving legs, the Bond Number is calculated to about 0.087, it indicates that surface tension

force dominates the lifting force and plays a major role in supporting the robot on water. Moreover, the characteristic velocity of the robot with flexible legs is closer to a water strider.

VI. CONCLUSION

In this study, flexible driving mechanism of water striders is studied. The force model and deformation model of the driving legs were established base on Bernoulli's beam theory. The influence of flexural rigidity and depth of a driving leg on the deformation and rowing speed is researched carefully. The theoretical results show that compared with rigid legs, flexible driving legs can row on water surface with a larger rowing velocity before penetrating the water surface. Then a new water strider robot that can walk on water surface was designed. The dynamic behavior of the robot is analyzed and then simulated by ADAMS software. The fabricated robot weighs 4.9 g and is supported by ten hydrophobic copper tubes. The driving legs are made of materials with different stiffness by 3D printing technology. Then a set of experiments and simulations were carried out to investigate the effect of rowing frequency and stiffness of the driving legs on the locomotion performance. The maximum forward and turning speeds of the robot with flexible driving legs can reach 139 mm/s and 24.8°/s respectively. The rowing frequency of the driving legs and the moving speed is more than 30% higher than the robot with rigid driving legs. Both experiments and simulations demonstrate that the rowing frequency of the driving legs and the moving speed are higher than the robot with rigid driving legs. Furthermore, a similarity analysis of hydrodynamic characteristic constants reveals that the characteristic velocity of the robot with flexible legs is closer to a water strider.

This paper has proved the effect of leg flexibility on improving the locomotion performance of the robot. As shown by the theoretical analysis and common sense, there exists an optimum stiffness for the driving legs. But limited by materials and fabrication method, the stiffness of the driving legs is difficult to be changed randomly. In this paper, we only studied the ABS material driving legs with elastic modulus of 2.3Gpa. In subsequent research, we will continue to optimize the mobility of the robot through exploring the optimum stiffness of flexible driving legs.

REFERENCES

[1] H. Mukundarajan, T. C. Bardon, D. H. Kim, and M. Prakash, "Surface tension dominates insect flight on fluid interfaces," *J. Experim. Biol.*, vol. 219, no. 5, pp. 752–766, Mar. 2016.

[2] B. Kwak and J. Bae, "Skimming and steering of a non-tethered miniature robot on the water surface using marangoni propulsion," in *Proc. IEEE/RSJ Int. Conf. Intell. Robots Syst. (IROS)*, Sep. 2017, pp. 3217–3222.

[3] J. W. Bush, D. L. Hu, and M. Prakash, "The integument of water-walking arthropods: Form and function," *Adv. Insect Physiol.*, vol. 34, pp. 92–117, Jan. 2007.

[4] D. L. Hu and J. W. M. Bush, "The hydrodynamics of water-walking arthropods," *J. Fluid Mech.*, vol. 644, pp. 5–33, Feb. 2010.

[5] B. Kwak and J. Bae, "Locomotion of arthropods in aquatic environment and their applications in robotics," *Bioinspiration Biomimetics*, vol. 13, no. 4, 2018, Art. no. 041002.

[6] X. Gao and L. Jiang, "Biophysics: Water-repellent legs of water striders," *Nature*, vol. 432, no. 7013, p. 36, Nov. 2004.

[7] D. L. Hu, B. Chan, and J. W. M. Bush, "The hydrodynamics of water strider locomotion," *Nature*, vol. 424, no. 6949, pp. 663–666, Aug. 2003.

[8] J. W. M. Bush and D. L. Hu, "Walking on water: Biolocomotion at the interface," *Annu. Rev. Fluid Mech.*, vol. 38, no. 1, pp. 339–369, Jan. 2006.

[9] D. L. Hu, M. Prakash, B. Chan, and J. W. Bush, "Water-walking devices," *Experim. Fluids*, vol. 43, pp. 769–778, Nov. 2007.

[10] Y. Seong Song and M. Sitti, "Surface-Tension-Driven biologically inspired water strider robots: Theory and experiments," *IEEE Trans. Robot.*, vol. 23, no. 3, pp. 578–589, Jun. 2007.

[11] Y. Seong Song, S. H. Suhr, and M. Sitti, "Modeling of the supporting legs for designing biomimetic water strider robots," in *Proc. IEEE Int. Conf. Robot. Autom. ICRA*, May 2006, pp. 2303–2310.

[12] S. H. Suhr, Y. S. Song, S. J. Lee, and M. Sitti, "Biologically inspired miniature water strider robot," in *Proc. Robot. Sci. Syst.* Cambridge, MA, USA: Massachusetts Institute of Technology, Jun. 2005, pp. 319–326.

[13] Y. S. Song and M. Sitti, "STRIDE: A highly maneuverable and non-tethered water strider robot," in *Proc. IEEE Int. Conf. Robot. Autom.*, Apr. 2007, pp. 980–984.

[14] O. Ozcan, H. Wang, J. D. Taylor, and M. Sitti, "STRIDE II: A water strider-inspired miniature robot with circular footpads," *Int. J. Adv. Robotic Syst.*, vol. 11, no. 6, p. 85, Jun. 2014.

[15] R. Girard, *Design Review#1: Water Strider*. New York, NY, USA: Columbia Univ., 2005.

[16] L. Wu, L. Ding, and D. Guo, "A bionic water strider robot," China Patent ZL.10 112 601.7, Apr. 25, 2006.

[17] L. Wu, Z. Lian, G. Yang, and M. Ceccarelli, "Water dancer II–A: A non-tethered telecontrollable water strider robot," *Int. J. Adv. Robotic Syst.*, vol. 8, no. 4, p. 39, Sep. 2011.

[18] J. H. Yan, X. B. Zhang, J. Zhao, G. F. Liu, H. G. Cai, and Q. M. Pan, "A miniature surface tension-driven robot using spatially elliptical moving legs to mimic a water strider's locomotion," *Bioinspiration Biomimetics*, vol. 10, no. 4, 2015, Art. no. 046016.

[19] X. Zhang, J. Zhao, Q. Zhu, N. Chen, M. Zhang, and Q. Pan, "Bioinspired aquatic microrobot capable of walking on water surface like a water strider," *ACS Appl. Mater. Interfaces*, vol. 3, no. 7, pp. 2630–2636, Jul. 2011.

[20] B. Shin, H.-Y. Kim, and K.-J. Cho, "Towards a biologically inspired small-scale water jumping robot," in *Proc. 2nd IEEE RAS EMBS Int. Conf. Biomed. Robot. Biomechtron.*, Oct. 2008, pp. 127–131.

[21] K. Suzuki, "Bio-inspired water strider robots with microfabricated functional surfaces," in *Biomimetics: Learning From Nature*, A. Mukherjee, Ed. Rijeka, Croatia: IntechOpen, 2010, pp. 363–383.

[22] S. Floyd and M. Sitti, "Design and development of the lifting and propulsion mechanism for a biologically inspired water runner robot," *IEEE Trans. Robot.*, vol. 24, no. 3, pp. 698–709, Jun. 2008.

[23] Q. Zheng, Y. Yu, and X.-Q. Feng, "The role of adaptive-deformation of water strider leg in its walking on water," *J. Adhes. Sci. Technol.*, vol. 23, no. 3, pp. 493–501, 2009.

[24] X.-Y. Ji, J.-W. Wang, and X.-Q. Feng, "Role of flexibility in the water repellency of water strider legs: Theory and experiment," *Phys. Rev. E, Stat. Phys. Plasmas Fluids Relat. Interdiscip. Top.*, vol. 85, no. 2, Feb. 2012, Art. no. 021607.

[25] D. Vella, "Floating objects with finite resistance to bending," *Langmuir*, vol. 24, no. 16, pp. 8701–8706, Aug. 2008.

[26] X. Q. Kong, J. L. Liu, W. J. Zhang, and Y. D. Qu, "Load-bearing ability of the mosquito tarsus on water surfaces arising from its flexibility," *AIP Adv.*, vol. 5, no. 3, Mar. 2015, Art. no. 037101.

[27] K. J. Park and H.-Y. Kim, "Bending of floating flexible legs," *J. Fluid Mech.*, vol. 610, pp. 381–390, Sep. 2008.

[28] S. Neukirch, B. Roman, B. de Gaudemaris, and J. Bico, "Piercing a liquid surface with an elastic rod: Buckling under capillary forces," *J. Mech. Phys. Solids*, vol. 55, no. 6, pp. 1212–1235, Jun. 2007.

[29] X.-Y. Ji and X.-Q. Feng, "Towards understanding elastocapillarity: Comparing wetting of soft and rigid plates," *J. Phys., Condens. Matter*, vol. 26, no. 15, Apr. 2014, Art. no. 155105.

[30] J.-L. Liu and X.-Q. Feng, "On elastocapillarity: A review," *Acta Mechanica Sinica*, vol. 28, no. 4, pp. 928–940, Aug. 2012.

[31] E. Yang, J. H. Son, S.-I. Lee, P. G. Jablonski, and H.-Y. Kim, "Water striders adjust leg movement speed to optimize takeoff velocity for their morphology," *Nature Commun.*, vol. 7, no. 1, p. 13698, Dec. 2016.

[32] M. Gauthier and M. Nourine, "Capillary force disturbances on a partially submerged cylindrical micromanipulator," *IEEE Trans. Robot.*, vol. 23, no. 3, pp. 600–604, Jun. 2007.
[33] J.-S. Koh, E. Yang, G.-P. Jung, S.-P. Jung, J. H. Son, S.-I. Lee, P. G. Jablonski, R. J. Wood, H.-Y. Kim, and K.-J. Cho, "Jumping on water: Surface tension-dominated jumping of water striders and robotic insects," *Science*, vol. 349, no. 6247, pp. 517–521, Jul. 2015.
[34] J. Yan, K. Yang, Y. Yang, J. Zhao, G. Liu, and S. Tang, "A new robot skating on water surface intimating water striders based on flexible driving mechanism*," in *Proc. Int. Conf. Robot. Autom. (ICRA)*, May 2019, pp. 2468–2473.
[35] *China*. Accessed: Feb. 19, 2019. [Online]. Available: https://v.qq.com/x/page/o0839n4wn1d.html
[36] D. Vella, D. G. Lee and H. Y. Kim, "Sinking of a horizontal cylinder," *Langmuir*, vol. 22, pp. 2972–2974, Mar. 2006.
[37] D. Vella, D. G. Lee and H. Y. Kim, "The load supported by small floating objects," *Langmuir*, vol. 22, pp. 5979–5981, Jul. 2006.
[38] Y. Zheng, H. Lu, W. Yin, D. Tao, L, Shi and Y. Tian, "Walking of spider on water surface studied from its leg shadows," *Chin. Phys. B*, vol. 27, no. 8, 2018, Art. no. 084702.
[39] L. Zhang, M. Zhao, Z, Wang, Y. Li, Y. Huang and Y. Zheng, "Measurement of dynamic force acted on water strider leg jumping upward by the PVDF film sensor," *J. Visualized Exp.*, vol. 138, Aug. 2018, Art. no. e58221.
[40] X. Zhang, J. Yan, J. Zhao, Y. Wang, and Q. Pan, "Vertical force acting on partly submerged spindly cylinders," *AIP Adv.*, vol. 4, no. 4, Apr. 2014, Art. no. 047118.

JIHONG YAN (Member, IEEE) received the B.S. and Ph.D. degrees in mechanical engineering from the Harbin Institute of Technology (HIT), Harbin, China, in 1997 and 2005, respectively.

She was engaged in research and development of the bionic robots, jumping robot, soft robotics, robotic control and manipulation, and space simulation facility. Since 2015, she has been a Professor with the State Key Laboratory of Robotics and Systems, HIT.

KAI YANG (Student Member, IEEE) received the B.S. degree in mechanical engineering and automation from the Ocean University of China, Shandong, China, in 2012, and the M.S. degree in mechanical engineering from the Harbin Institute of Technology (HIT), Harbin, China, in 2014, where he is currently pursuing the Ph.D. degree with the State Key Laboratory of Robotics and System.

His research interests include bionic water sliding robots and mechanism design.

GANGFENG LIU (Member, IEEE) received the B.S. and Ph.D. degrees in mechanical engineering from the Harbin Institute of Technology (HIT), Harbin, China, in 2005 and 2010, respectively.

He was engaged in research and development of the robot for special environment, robotic control and manipulation, and space simulation facility.

JIE ZHAO (Member, IEEE) received the B.S. and Ph.D. degrees in mechatronics engineering from the Harbin Institute of Technology (HIT), Harbin, China, in 1990 and 1996, respectively.

He is currently a Professor with the School of Mechatronics Engineering, HIT. He is the Head of the Robotics Institute and the School of Mechatronics Engineering, HIT. He is also the Leader of the Subject Matter Expert Group of Intelligent Robot in National 863 Program supervised by the Ministry of Science and Technology of China. His research interests include industrial robots and bionic robots.